Earthquakes and Structures, *Vol. 13, No. 5 (2017) 455-464*
DOI: https://doi.org/10.12989/eas.2017.13.5.455

An ESED method for investigating seismic behavior of single-layer spherical reticulated shells

Ming Zhang*[1], Guangchun Zhou[2], Yanxia Huang[1], Xudong Zhi[2] and De-Yi Zhang[1]

[1]*School of Civil Engineering, Southwest Jiaotong University, Chengdu 610031, China*
[2]*School of Civil Engineering, Harbin Institute of Technology, 73 Huanghe Road, Harbin, 150090, China*

(Received January 4, 2017, Revised December 10, 2017, Accepted December 11, 2017)

Abstract. This paper develops a new method for analyzing the structural seismic behavior of single-layer reticulated shells based on exponential strain energy density (ESED). The ESED method reveals a characteristic point from a relationship between ESED sum and peak seismic acceleration. Then, the characteristic point leads to an updated concept of structural failure and an ESED-based criterion for predicting structural failure load. Subsequently, the ESED-based criterion and the characteristic point are verified through numerical analysis of typical single-layer reticulated shells with different configurations and a shaking table test of the scale shell model. Finally, discussions further verify the rationality and application of the ESED-based criterion. The ESED method might open a new way of structural analysis and the ESED-based criterion might indicate a prospect for a unified criterion for predicting seismic failure loads of various structures.

Keywords: ESED method; ESED-based criterion; failure load; single-layer spherical shell; characteristic point

1. Introduction

Single-layer reticulated shells have been widely used in spatial structures in recent decades (Yu *et al*. 2011, Bai *et al*. 2015) because of their advantages, such as aesthetic appearance, large space and sound mechanical performance. Current research work is mainly focused on structural response (Liu and Li 2010, Zhai *et al*. 2013, Nie *et al*. 2014, Kong *et al*. 2014, Li *et al*. 2014, Fan *et al*. 2014, Ma *et al*. 2014), collapse (Ye *et al*. 2011, Ye *et al*. 2011, Liu and Ye 2014) of the space steel structure under different loads through experiment and numerical simulation analysis (Zhu and Ye 2014, Yan *et al*. 2014, Ma *et al*. 2015, Ba *et al*. 2015, Zhong *et al*. 2016), stability and buckling (Fan *et al*. 2010, Ramalingam and Jayachandran 2015, Bruno *et al*. 2016, Yan *et al*. 2016). Only limited researches have been conducted to investigate the structural failure mechanism (Ba *et al*. 2015, Zhi *et al*. 2007, Zhi *et al*. 2010, Fan *et al*. 2010), and the seismic failure modes of single-layer reticulated shells are divided into, dynamic instability and strength failure modes, two types. Based on the two failure modes, Zhi *et al*. (2007) empirically proposed two different criteria for predicting the failure loads of single-layer reticulated shells and cylindrical reticulated shells through analyzing the maximum nodal displacement and structural plastic deformation. In addition, a convergence criterion used in the finite element analysis (FEA) is also proposed to terminate the numerical simulation according to mechanical requirement or arithmetic limitation, such as the tolerance of force based on the force imbalance and the tolerance of displacement based on the difference between displacements (Chong 1993). However, all the existing dynamical criteria are empirical and statistical lacking mechanical basis. Worse yet, the existing criteria are independent for different failure modes, and some failure modes are difficult to disguise dynamic instability from strength failure. Therefore, a further study should be performed in this area to reveal some unseen knowledge implied in a huge amount of simulative data to pursue a rational and unified criterion for accurately predicting structural failure load.

Like the structural energy concept used by Paolacci (2013), Shehata *et al*. (2013), Maria *et al*. (2014), the global seismic behavior of single-layer reticulated shells is investigated based on exponential strain energy density (ESED). The aim is to construct a more rational and unified failure criterion to aid design engineers to construct higher reliable single-layer reticulated shells.

2. ESED Method and ESED-based criterion

The parameter of ESED plays a key role in the process of investigating seismic behavior of single-layer reticulated shells and studying the new failure criterion (ESED-based criterion), hence it is necessary to firstly introduce the ESED method. For clearly, the ESED method is divided into the following steps:

(1) Transform the strain energy density (SED) values extracting from the FEA results into the ESED values and calculate the sum (I_d) of the ESED values;

(2) Explore a relationship between the I_d and the load intensity to reveal the characteristic of structural working state;

(3) Establish the ESED-based criterion for predicting the

*Corresponding author, Ph.D.
E-mail: zhangming@home.swjtu.edu.cn

ISSN: 2092-7614 (Print), 2092-7622 (Online)

structural failure load according to the characteristic revealed in the step (2);

(4) Clarify the rationality, unity and applicability of the ESED-based criterion.

2.1 Calculation of ESED values

Owing to the bilinear kinematic hardening elastic-plastic model adopted in this study to describe nonlinear material property, structural strain energy can be divided into the elastic and plastic parts. Therefore, for the ith element to the *j*th integration point, its strain energy G^i can be written as

$$G^i = \frac{1}{2}\sum_{j=1}^{n}\left(\left((\boldsymbol{\sigma}_j^i)^e\right)^T(\boldsymbol{\varepsilon}_j^i)^e + \left((\boldsymbol{\sigma}_j^i)^p\right)^T(\boldsymbol{\varepsilon}_j^i)^p\right)v_j^i \tag{1}$$

where $(\boldsymbol{\sigma}_j^i)^e = [\sigma_{xx}^e\ \sigma_{yy}^e\ \sigma_{zz}^e\ \tau_{xy}^e\ \tau_{yz}^e\ \tau_{zx}^e]^T$ and $(\boldsymbol{\varepsilon}_j^i)^e = [\varepsilon_{xx}^e\ \varepsilon_{yy}^e\ \varepsilon_{zz}^e\ \gamma_{xy}^e\ \gamma_{yz}^e\ \gamma_{zx}^e]^T$ are the elastic stress and strain vectors; $(\boldsymbol{\sigma}_j^i)^p = [\sigma_{xx}^p\ \sigma_{yy}^p\ \sigma_{zz}^p\ \tau_{xy}^p\ \tau_{yz}^p\ \tau_{zx}^p]^T$ and $(\boldsymbol{\varepsilon}_j^i)^p = [\varepsilon_{xx}^p\ \varepsilon_{yy}^p\ \varepsilon_{zz}^p\ \gamma_{xy}^p\ \gamma_{yz}^p\ \gamma_{zx}^p]^T$ are the plastic stress and strain vectors; $((\boldsymbol{\sigma}_j^i)^e)^T$ and $((\boldsymbol{\sigma}_j^i)^p)^T$ are the transposed matrixes of $(\boldsymbol{\sigma}_j^i)^e$ and $(\boldsymbol{\sigma}_j^i)^p$; v_j^i is the volume; n is the number of integration points; $\sigma_{xx}^e, \sigma_{xx}^p, \sigma_{yy}^e, \sigma_{yy}^p, \sigma_{zz}^e, \sigma_{zz}^p$, $\tau_{xy}^e, \tau_{xy}^p, \tau_{yz}^e, \tau_{yz}^p, \tau_{zx}^e$ and τ_{zx}^p are the normal stresses and shear stresses and the corresponding strains are $\varepsilon_{xx}^e, \varepsilon_{xx}^p$, ε_{yy}^e, ε_{yy}^p, ε_{zz}^e, ε_{zz}^p, γ_{xy}^e, γ_{xy}^p, γ_{yz}^e, γ_{yz}^p, γ_{zx}^e and γ_{zx}^p; $\frac{1}{2}\sum_{j=1}^{n}\left((\boldsymbol{\sigma}_j^i)^e\right)^T(\boldsymbol{\varepsilon}_j^i)^e v_j^i$ and $\frac{1}{2}\sum_{j=1}^{n}\left((\boldsymbol{\sigma}_j^i)^p\right)^T(\boldsymbol{\varepsilon}_j^i)^p v_j^i$ are the elastic and plastic strain energy. The relationship between the stress and the strain in Eq. (1) are generally written as (Owen and Hinto 1980)

$$(\boldsymbol{\sigma}_j^i)^e = (\mathbf{D}_j^i)^e(\boldsymbol{\varepsilon}_j^i)^e; \quad (\boldsymbol{\sigma}_j^i)^p = (\mathbf{D}_j^i)^p(\boldsymbol{\varepsilon}_j^i)^p \tag{2}$$

where $(\mathbf{D}_j^i)^e$ and $(\mathbf{D}_j^i)^p$ are the elastic and elasto-plastic stress-strain matrixes from the bilinear kinematic hardening elasto-plastic model of steel.

Now, we express the stress and strain using the equivalent mass matrix $\mathbf{m}_j^i$ and the stress relation matrix $\mathbf{S}_j^i$ as well as the seismic peak acceleration A for same seismic wave with different peak acceleration, in order to reveal the characteristic of structural working behavior. The transformation of this expression is derived as the following three steps:

(1) Construct the inertia force vector $\mathbf{F}_j^i$ (Chopra 1995)

$$\mathbf{F}_j^i = -\mathbf{m}_j^i \boldsymbol{\iota} A \tag{3}$$

where the influence vector $\boldsymbol{\iota}$ represents the displacements of the masses resulting from static application of a unit ground displacement. The stress and strain vectors $(\boldsymbol{\sigma}_j^i)^e$, $(\boldsymbol{\sigma}_j^i)^p$, $(\boldsymbol{\varepsilon}_j^i)^e$ and $(\boldsymbol{\varepsilon}_j^i)^p$ can be directly expressed through $\mathbf{F}_j^i$ and the stress-strain relation matrix $\mathbf{S}_j^i$. If the equivalent stress $f(\boldsymbol{\sigma}_j^i)$ is less than the material yield strength σ_y, then

$$(\boldsymbol{\sigma}_j^i)^e = \mathbf{S}_j^i\mathbf{F}_j^i, \text{ and } (\boldsymbol{\sigma}_j^i)^p = \mathbf{0} \tag{4}$$

$$(\boldsymbol{\varepsilon}_j^i)^e = \left((\mathbf{D}_j^i)^e\right)^{-1}(\boldsymbol{\sigma}_j^i)^e, \text{ and } (\boldsymbol{\varepsilon}_j^i)^p = \mathbf{0} \tag{5}$$

where $\mathbf{S}_j^i = \mathbf{D}_j^i\mathbf{B}_j^i(\mathbf{K}_j^i)^{-1}$ is the stress relation matrix (Owen and Hinto 1980, Chopra 1995); $\mathbf{B}_j^i$ and $\mathbf{K}_j^i$ are the strain relation matrix and the stiffness matrix. When $f(\boldsymbol{\sigma}_j^i) > \sigma_y$, then

$$(\boldsymbol{\sigma}_j^i)^e = (\boldsymbol{\sigma}_j^i)_y \text{ and } (\boldsymbol{\sigma}_j^i)^p = \mathbf{S}_j^i\mathbf{F}_j^i - (\boldsymbol{\sigma}_j^i)_y^e \tag{6}$$

where $(\boldsymbol{\sigma}_j^i)_y$ is the stress vector when $f(\boldsymbol{\sigma}_j^i)=\sigma_y$. The elastic and plastic strain vectors corresponding to Eq. (6) can be written as

$$(\boldsymbol{\varepsilon}_j^i)^e = \left((\mathbf{D}_j^i)^e\right)^{-1}(\boldsymbol{\sigma}_j^i)_y,\ (\boldsymbol{\varepsilon}_j^i)^p = \left((\mathbf{D}_j^i)^p\right)^{-1}(\boldsymbol{\sigma}_j^i)^p \tag{7}$$

where $((\mathbf{D}_j^i)^e)^{-1}$ and $((\mathbf{D}_j^i)^p)^{-1}$ are the inverse matrixes of $(\mathbf{D}_j^i)^e$ and $(\mathbf{D}_j^i)^p$.

(2) Consider the initial imperfections $(\boldsymbol{\delta}_j^i)^e$ and $(\boldsymbol{\delta}_j^i)^p$ of the *i*th element to the integration point *j*, then $(\boldsymbol{\varepsilon}_j^i)^e$, $(\boldsymbol{\varepsilon}_j^i)^p$, $(\boldsymbol{\sigma}_j^i)^e$ and $(\boldsymbol{\sigma}_j^i)^p$ can re-written as

$$(\tilde{\boldsymbol{\varepsilon}}_j^i)^e = (\boldsymbol{\varepsilon}_j^i)^e + (\boldsymbol{\delta}_j^i)^e, \quad (\tilde{\boldsymbol{\varepsilon}}_j^i)^p = (\boldsymbol{\varepsilon}_j^i)^p + (\boldsymbol{\delta}_j^i)^p \tag{8}$$

$$(\tilde{\boldsymbol{\sigma}}_j^i)^e = (\mathbf{D}_j^i)^e(\tilde{\boldsymbol{\varepsilon}}_j^i)^e, \quad (\tilde{\boldsymbol{\sigma}}_j^i)^p = (\mathbf{D}_j^i)^p(\tilde{\boldsymbol{\varepsilon}}_j^i)^p \tag{9}$$

Hereto, the strain energy $\tilde{G}^i$ of the *i*th element can be obtained in consideration of the initial imperfections

$$\tilde{G}^i = \frac{1}{2}\sum_{j=1}^{n}\left(\left((\tilde{\boldsymbol{\sigma}}_j^i)^e\right)^T(\tilde{\boldsymbol{\varepsilon}}_j^i)^e + \left((\tilde{\boldsymbol{\sigma}}_j^i)^p\right)^T(\tilde{\boldsymbol{\varepsilon}}_j^i)^p\right)v_j^i \tag{10}$$

where the strain energy $\tilde{G}^i$ is taken at the end of the duration of a selected wave. If v_j^i is treated as the same to all integration points, the normalized form I^i of $\tilde{G}^i$ can be written in Eq. (11).

$$I^i = \frac{\tilde{G}^i}{\sum_{j=1}^{n} v_j^i} = \frac{\tilde{G}^i}{n \cdot v_j^i} \tag{11}$$

Substituting Eq. (10) into Eq. (11) yields

$$I^i = \frac{1}{2n}\sum_{j=1}^{n}\left(\left((\tilde{\boldsymbol{\sigma}}_j^i)^e\right)^T(\tilde{\boldsymbol{\varepsilon}}_j^i)^e + \left((\tilde{\boldsymbol{\sigma}}_j^i)^p\right)^T(\tilde{\boldsymbol{\varepsilon}}_j^i)^p\right) \tag{12}$$

where $\left((\tilde{\boldsymbol{\sigma}}_j^i)^e\right)^T$ and $\left((\tilde{\boldsymbol{\sigma}}_j^i)^p\right)^T$ are the transposed matrixes of $(\tilde{\boldsymbol{\sigma}}_j^i)^e$ and $(\tilde{\boldsymbol{\sigma}}_j^i)^p$. Then, by substituting Eqs. (4)-(9) into Eq. (12), the direct relationship between I^i and A can be expressed as

$$\begin{aligned} I^i = \frac{1}{2n}\sum_{j=1}^{n}\Bigg(& \left(\mathbf{m}_j^i\boldsymbol{\iota}\right)^T\left(\mathbf{S}_j^i\right)^T\left(\left(\mathbf{D}_j^i\right)^e\right)^{-1}\mathbf{S}_j^i\mathbf{m}_j^i\boldsymbol{\iota} \\ & + \left(\mathbf{m}_j^i\boldsymbol{\iota}\right)^T\left(\mathbf{S}_j^i\right)^T\left(\left(\mathbf{D}_j^i\right)^p\right)^{-1}\mathbf{S}_j^i\mathbf{m}_j^i\boldsymbol{\iota}\Bigg)A^2 \\ & -\Bigg(\left(\mathbf{m}_j^i\boldsymbol{\iota}\right)^T\left(\mathbf{S}_j^i\right)^T\left(\boldsymbol{\delta}_j^i\right)^e + \left(\left(\boldsymbol{\delta}_j^i\right)^e\right)^T\left(\left(\mathbf{D}_j^i\right)^e\right)^T\left(\left(\mathbf{D}_j^i\right)^e\right)^{-1}\mathbf{S}_j^i\mathbf{m}_j^i\boldsymbol{\iota} \\ & -\left(\mathbf{m}_j^i\boldsymbol{\iota}\right)^T\left(\mathbf{S}_j^i\right)^T\left(\left(\mathbf{D}_j^i\right)^p\right)^{-1}\left(\boldsymbol{\sigma}_j^i\right)_y + \left(\mathbf{m}_j^i\boldsymbol{\iota}\right)^T \\ & \left(\mathbf{S}_j^i\right)^T\left(\boldsymbol{\delta}_j^i\right)^p - \left(\left(\boldsymbol{\sigma}_j^i\right)_y\right)^T\left(\left(\mathbf{D}_j^i\right)^p\right)^{-1}\mathbf{S}_j^i\mathbf{m}_j^i\boldsymbol{\iota}\Bigg)A \\ & + \left(\left(\boldsymbol{\delta}_j^i\right)^e\right)^T\left(\left(\mathbf{D}_j^i\right)^e\right)^T\left(\boldsymbol{\delta}_j^i\right)^e + \left(\left(\boldsymbol{\sigma}_j^i\right)_y\right)^T \end{aligned}$$

$$\left(\left(\mathbf{D}_j^i\right)^p\right)^{-1}\left(\boldsymbol{\sigma}_j^i\right)_y-\left(\left(\boldsymbol{\sigma}_j^i\right)_y\right)^T\left(\boldsymbol{\delta}_j^i\right)^p \tag{13}$$

Furthermore, we obtain the relationship between I^i and A

$$2nI^i=a^iA^2+b^iA+c^i \tag{14}$$

where

$$a^i=\sum_{j=1}^{n}\left(\left(\mathbf{m}_j^i\mathbf{1}\right)^T\left(\mathbf{S}_j^i\right)^T\left(\left(\mathbf{D}_j^i\right)^p\right)^{-1}\mathbf{S}_j^i\mathbf{m}_j^i\mathbf{1}+\left(\mathbf{m}_j^i\mathbf{1}\right)^T\left(\mathbf{S}_j^i\right)^T\left(\left(\mathbf{D}_j^i\right)^p\right)^{-1}\mathbf{S}_j^i\mathbf{m}_j^i\mathbf{1}\right)$$

$$b^i=-\sum_{j=1}^{n}\left(\left(\mathbf{m}_j^i\mathbf{1}\right)^T\left(\mathbf{S}_j^i\right)^T\left(\boldsymbol{\delta}_j^i\right)^e+\left(\left(\boldsymbol{\delta}_j^i\right)^e\right)^T\left(\left(\mathbf{D}_j^i\right)^e\right)^T\left(\left(\mathbf{D}_j^i\right)^e\right)^{-1}\mathbf{S}_j^i\mathbf{m}_j^i\mathbf{1}$$

$$-\left(\mathbf{m}_j^i\mathbf{1}\right)^T\left(\mathbf{S}_j^i\right)^T\left(\left(\mathbf{D}_j^i\right)^p\right)^{-1}\left(\boldsymbol{\sigma}_j^i\right)_y+\left(\mathbf{m}_j^i\mathbf{1}\right)^T\left(\mathbf{S}_j^i\right)^T\left(\boldsymbol{\delta}_j^i\right)^p-\left(\left(\boldsymbol{\sigma}_j^i\right)_y\right)^T\left(\left(\mathbf{D}_j^i\right)^p\right)^{-1}\mathbf{S}_j^i\mathbf{m}_j^i\mathbf{1}\Big)$$

$$c^i=\left(\left(\boldsymbol{\delta}_j^i\right)^e\right)^T\left(\left(\mathbf{D}_j^i\right)^e\right)^T\left(\boldsymbol{\delta}_j^i\right)^e+\left(\left(\boldsymbol{\sigma}_j^i\right)_y\right)^T\left(\left(\mathbf{D}_j^i\right)^p\right)^{-1}\left(\boldsymbol{\sigma}_j^i\right)_y-\left(\left(\boldsymbol{\sigma}_j^i\right)_y\right)^T\left(\boldsymbol{\delta}_j^i\right)^p$$

(3) Derive the new parameter I_d from the normalized strain energy parameter I^i

$$I_d=\sum_{i=1}^{N}\sqrt{2nI^i}\ =f(A) \tag{15}$$

where N is the number of structural elements and $\sqrt{2nI^i}$ is the ESED value of the ith element; $f(A)$ indicates that I_d as the sum of ESED values is the function of A. It should be indicated that both elastic and plastic strain energy is taken at the end of the time history for a given ground motion input. Hence, I_d is also calculated as the sum of the ESED values of all the members at the end of the acceleration time history. This is due to the fact that plastic strain energy accumulates throughout the time history of the ground motion and is also a predominant indicator of structural failure state.

So far, the new parameter, I_d, has been derived to reflect global structural working state, according to two reasons: (1) I_d as a scalar quantity contains the state values (ESED values) at all the elements consisting of the structure; (2) the exponential form of SED value would lead to more linear correlation with A. Thus, an analysis of the working state characteristic for single-layer reticulated shells can be conducted through the I_d-A curve in the following section.

2.2 Characteristic points in the I_d-A curve

Shell D40207 is taken as an example to demonstrate the characteristic of structural working state implied in the I_d-A curve. The configuration parameters of Shell D40207 are listed in Table 1 below. To highlight the characteristic of structural working state, Shell D40207 is subjected to the harmonic excitation with 5Hz frequency. In the I_d-A curve shown in Fig. 1, there are two characteristic points, Points P and U, corresponding to the ground accelerations of 4.72 m/s^2 and 20.5 m/s^2, respectively. Point P is the turning point that the structural behavior evolves from elastic to elastic-plastic. Usually, Point P is not obvious in the I_d-A curve, but it can be determined in the FEA simulation. Point U indicates the boundary point that the structure behavior entering the unstable working state. Generally, Point U can be identified in the I_d-A curve as that the I_d will dramatically increase when the A reaches its failure load. Points P and U characterize three stages of structural working state: (1) Before Point P, all the elements are in the elastic state,

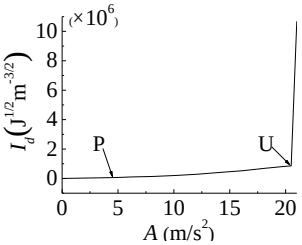

Fig. 1 Characteristic points in the I_d-A curve

showing the linear correlation between I_d and A. Also, the structure is in normal working state; (2) From Point P to Point U, the number of structural elements entering their elastic-plastic state gradually increases, showing a stable nonlinear correlation between I_d and A. In this stage, the structure is still in normal working state; (3) After Point U, the structure enters its unstable working state, showing an unstable nonlinear correlation between I_d and A.

Generally, the existing concept of structural failure is structural collapse corresponding to structural ultimate limit load. However, this study implies that the structural working state before Point U is different from that after Point U; in other words, the structural working state after Point U can be judged to be unstable with the increment of the peak acceleration A, from the tendency the I_d-A curve. Therefore, the concept of structural failure can be updated to correspond to the Point U. Or rather, structural failure (after Point U) is updated as a structure loses its normal/stable working state and the corresponding load at Point U is called as structural failure load. Moreover, it should be noted that structural failure defined by Point U is different from structural collapse corresponding to the loss of structural load-bearing capacity. Structural failure updated in this study suggests that although a structure loses its stable working state, it can still bear greater load in an unstable and changeable working state. Structural collapse indicates that the structure even loses its unstable and changeable working state, that is, the structure loses its ultimate load-bearing capacity so that it cannot bear greater load.

2.3 ESED-based criterion for predicting the failure load

The Point U can distinguish a structure normal working state from its failure state as previously described, therefore an ESED-base criterion can be derived to predict the structural failure load corresponding to Point U. The ESED-base criterion is defined as

$$k_i=\frac{\left(I_{d,i}-I_{d,1}\right)\max\left(A_i\right)}{\left(A_i-A_1\right)\max\left(I_{d,i}\right)}\geq 1 \tag{16}$$

where k_i is the slope of the I_d-A curve segment between the ith and 1st acceleration amplitudes, A_i and A_1. Here, k_i is also considered as a structural failure index. Equation (16) is termed as the ESED-based criterion for predicting structural failure load. Actually, the tendency of k-A curve, as shown in Fig. 2, is consistent with that of I_d-A curve in Fig. 1.

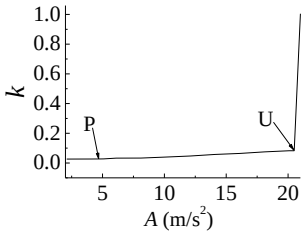

Fig. 2 Relationship between the k and A

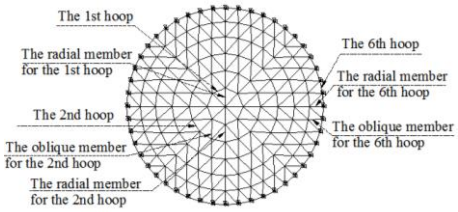

(a) Configuration of the shell

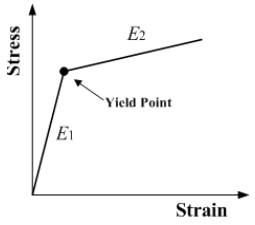

(b) Bilinear kinematic hardening model

Fig. 3 FEA model of a shell using the Kiewitt system

3. Numerical verification of the characteristic point

To further verify whether or not the characteristic point U universally exists in the change of structural working state, nine typical shells undergoing the TAFT earthquake wave are investigated by the ANSYS program. The nine shells have different rise-span ratios, spans and cross section areas of members. Fig. 3(a) shows the FEA model of a typical K8 single-layer spherical reticulated shell. The K8 shell is a Kiewitt system which has the eight parts uniformly divided by the eight radius lines from the center of the shell surface. Other details of the K8 single-layer reticulated shell were shown in Zhi's paper (Zhi *et al.* 2007). Similarly, the K6 shell is also a Kiewitt system with six divided parts, as shown in Fig. 5 below. It was assumed that all the supports of the shell models fixed against translation but free for rotation; the joints between the members were taken as rigid. The lumped mass at the node in the FEA model was described by a point element of MASS21, which could be calculated from the given roof weight. Both geometrical and material nonlinearities were considered in the dynamic analysis. The material of the shell was steel whose bilinear kinematic hardening elastic-plastic model is illustrated in Fig. 3(b). Here, the model had the yield stress of 235 MPa, Young's modulus E_1 (initial slope) of 2.06×10^5 MPa and Young's modulus E_2 (the second slope) of $0.02E_1$. The Rayleigh damping was composed of the first and second natural vibration frequencies in the case that the damping ratio was set as 0.02 empirically. The input seismic motion was the three-dimensional TAFT wave with a duration of 20s. Nonlinear time-history response was simulated using the finite-element package ANSYS. The PIPE20 element with six degrees of freedom (U_x, U_y, U_z, θ_x, θ_y and θ_z) at each node was adopted to represent the displacements for the members in the shell, and each single element was uniformly divided into three segments along the respective length. The convergence criterion in the FEA simulation was based on *TOF* (*TOF*=0.5%) and *TOD* (*TOD*=5%) (Chong 1993) as shown in Eq. (18) below. The FEA output includes nodal displacements, element stress and strain values, and strain energy. More information about the structural model is provided in Table 1.

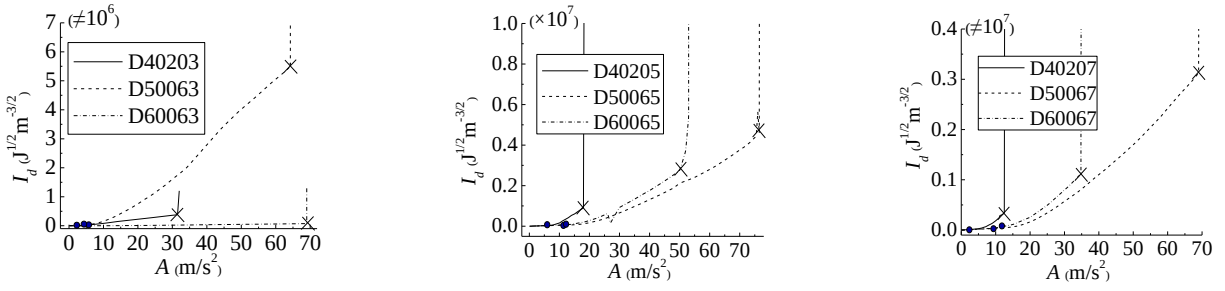

(a) The I_d-A curves

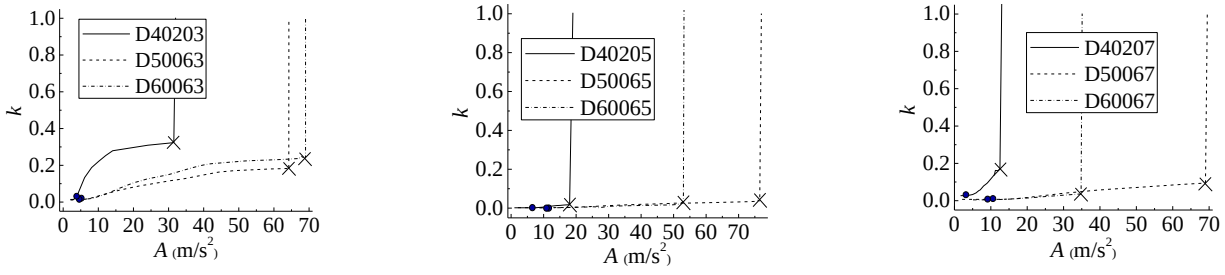

(b) The k-A curves

Fig. 4 The relationship of A with I_d and k for the selected shell.

Table 1 Labels and parameters of the shell models

Shell label	Span (m)	Roof weight (kg/m^2)	Rise to span ratio	Cross section (mm)	
				Radial and hoop members	Oblique members
D40203	40	200	1/3	146×5	140×6
D40205	40	200	1/5	146×5	140×6
D40207	40	200	1/7	146×5	140×6
D50063	50	60	1/3	168×6	152×5
D50065	50	60	1/5	168×6	152×5
D50067	50	60	1/7	168×6	152×5
D60063	60	60	1/3	194×6	168×6
D60065	60	60	1/5	194×6	168×6
D60067	60	60	1/7	194×6	168×6

Note: The 'Shell label' is the designation of single-layer reticulated domes defined by Zhi *et al*. (2007). For the name of Shell D40203, *D* indicates shell/dome, 40 is its span (40 m), 20 is its roof weight (200 kg/m^2) and 3 is its reciprocal of rise to span ratio.

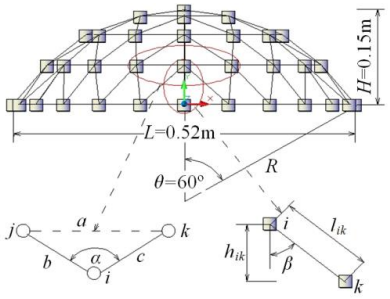

(a) Side view

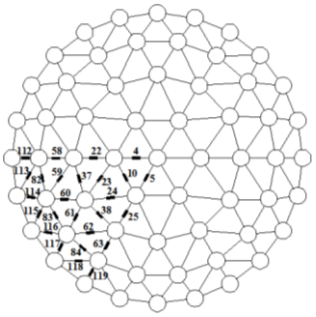

(b) Plan view

Fig. 5 The experimental K6 shell model

After obtaining the FEA output of the single-layer reticulated shells, the I_d-A and k-A curves of the nine shells are plotted respectively, as shown in Fig. 4(a) and (b). Fig. 4(a) illustrates that all the I_d-A curves present their characteristic points P (the mark '·') and U (the mark '×'); correspondingly, the characteristic points also exist in the k-A curves. Hence, the ESED-based method reveals the characteristic of structural working state and the ESED-based criterion reflect this characteristic.

4. Experimental verification

The ESED method depends on the FEA accuracy, as the ESED values are derived from the FEA simulation of shells.

Table 2 The natural frequencies of the experimental and simulative K6 shell model

Natural Frequencies	Experimental model (Hz)	FEA model (Hz)	Error (%)
f_1	8.73	8.59	1.60
f_2	9.72	9.25	4.84
f_3	10.29	10.82	5.15
f_4	11.10	11.04	0.54
f_5	11.71	11.21	4.30

Therefore, an experimental model was built to validate the FEA model of the shell and the characteristic point. The scale model was a small K6 shell model with the span (L) of 0.52 m and the height (H) of 0.15 m as shown in Fig. 5(a). For each seismic load, the dynamical strains of the members were recorded by the strain gauges whose positions on the model are shown in Fig. 5(b). Further, the assembly of experimental specimens is shown in Fig. 6.

As Fig. 6 shows, the assembly of the K6 shell model is as follows: (1) 304 stainless steel pipes have the same cross section size of Φ1.5×0.15. The yield stress and Young's modulus of the stainless steel pipe were measured experimentally; (2) The cylinder-shaped steel lumps serving as joints have the same height and diameter of 20 mm, and the same weight of 0.05 kg; (3) Every lead lump served as additional weight of 0.4847 kg. The steel joint was designed as a hole-glued joint. The stainless steel pipes were inserted into the holes in the steel lump, and the joint was then formed by gluing the steel pipes and the steel lump together. The material parameters of the 304 stainless steel pipe were quantified through six standard tensile experiments in the laboratory. The results showed that the average yield stress for the steel pipes was 255 MPa, and the Young's moduli were 1.89×10^5 MPa and 2.7×10^3 MPa in the elastic and plastic stages, respectively. In addition, the damping ratio of the experimental model was identified to be 0.04 using the free vibration test.

The natural frequencies of the scale model are shown in Table 2 obtained from the experiment and the FEA simulation as well as the corresponding errors. The FEA frequencies are highly near to the experimental frequencies. Then, the experiment of the K6 shell model was conducted under horizontal harmonic excitation with the frequency of 9.6 Hz close to the natural frequency of the model. The intensity of the input harmonic excitation (i.e., the acceleration amplitude) was gradually increased from 0.15 m/s^2 to 6 m/s^2. The progressive collapse of the model was from the 4th hoop to the 1st hoop, and the collapse mode is shown in Fig. 7(a), (b) and (c). This collapse process is nearly identical to the FEA result for Shell D40207 (Fig. 9(a) in the next section). And, the failure state of a typical member in the K6 shell model is shown in Fig. 7(d).

The experimental and FEA time-displacement history curves of the top node under an acceleration amplitude of 0.15 m/s^2 are shown in Fig. 8(a) which are close to each other in peak displacements basically. Corresponding to Fig. 8(a), Fig. 8(b) shows the experimental and FEA I_d-A curves of the model. The mean error between the I_d-A curves from the experiment and the FEA simulation is

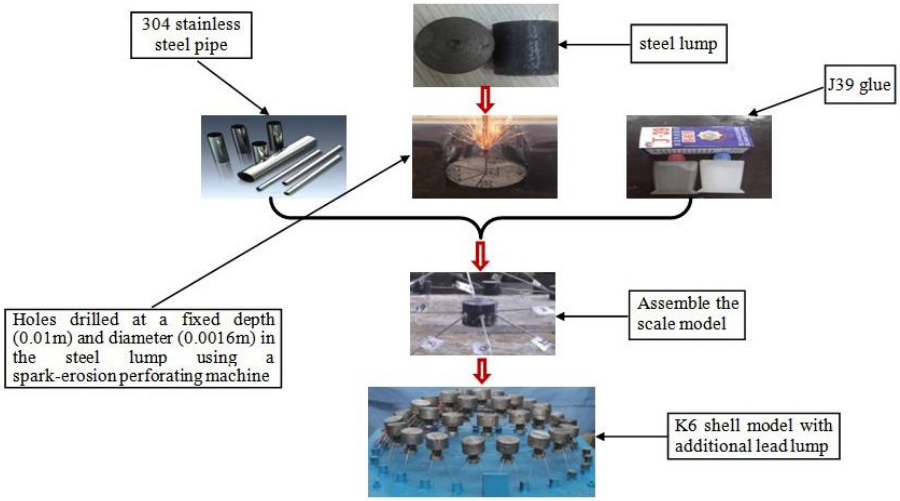

Fig. 6 The assembly of the K6 shell model

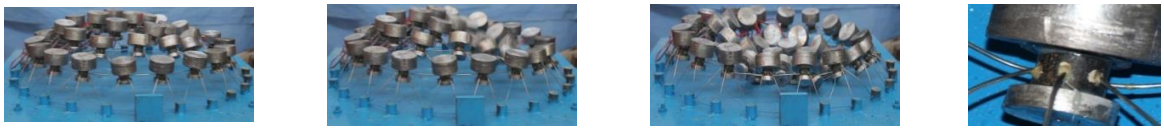

(a) First collapse (b) Further collapse (c) Final Collapse (d) Failure node

Fig. 7 The collapse process of the K6 shell model in the experiment

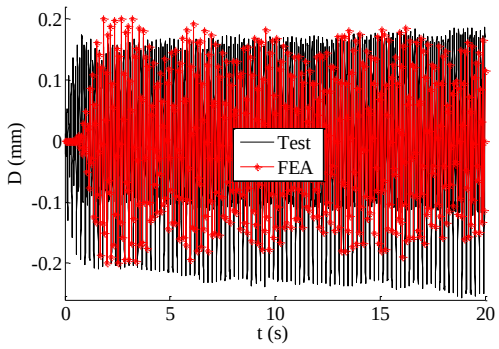

(a) The experimental and simulative displacements under an acceleration amplitude of 0.15 m/s^2

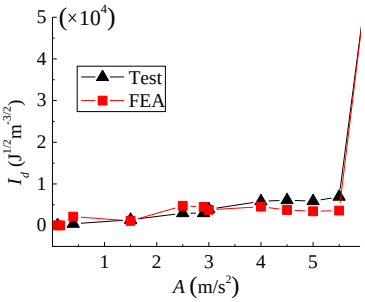

(b) The experimental and simulative I_d-A curves

Fig. 8 The experimental and FEA results for the K6 shell model

11.36%.

In general, the experimental results, including the natural frequencies, the progressive collapse, the top nodal dynamic displacement as well as the structural I_d-A curves, could verify the existence of the characteristic point U basically.

5. Discussion

5.1 Implication of structural failure load and I_d

As defined above, structural failure load is certainly lower than or equal to the structural collapse load. To elucidate this point, the FEA and ESED-based analysis of Shell D40207 is illustrated in Fig. 9. The progressive collapse of Shell D40207 is shown in Fig. 9(a). The relationship between I_d and A for Shell D40207 under the harmonic excitation with 5 Hz frequency is shown in Fig. 9(b). The relationship between the maximum nodal displacement D and the peak acceleration A is shown in Fig. 9(c). The SED values for all elements corresponding to the A values are shown in Fig. 9(d).

From Fig. 9(b), it can be seen that the characteristic points, the structural failure point U and the structural collapse point U', emerge in the I_d–A. But the structural failure point U does not emerge in Fig. 9(c). Thus, two features can be drawn from Figs. 9(b) and (c): (1) Shell D40207 collapses when the peak acceleration A reaches 23.0 m/s^2 (Point U'). Following the emergence of Point U', the structural displacement D sharply increases, and the structural deformation mode changes significantly. (2) Point U' appears in Figs. 9(b) and (c), but Point U does not appear in Fig. 9(c). This phenomenon indicates that I_d is more sensitive than D to the change of structural working state. Or rather, I_d as a structural parameter could reflect the characteristic of structural working behavior more than does the local maximum displacement D. The two features mentioned above further verify the definiteness that Point U is the structural failure point and the corresponding peak acceleration A is the structural failure load. However, this

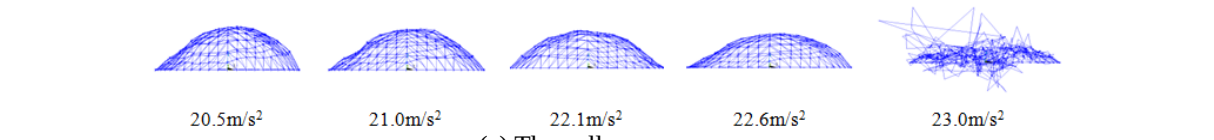

(a) The collapse process

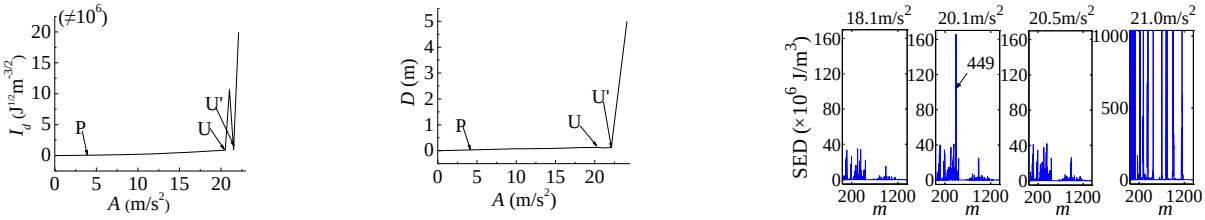

(b) The I_d-A curve (c) The D-A curve (d) The SED values for all elements

Fig. 9 The FEA and ESED-based analysis of Shell D40207

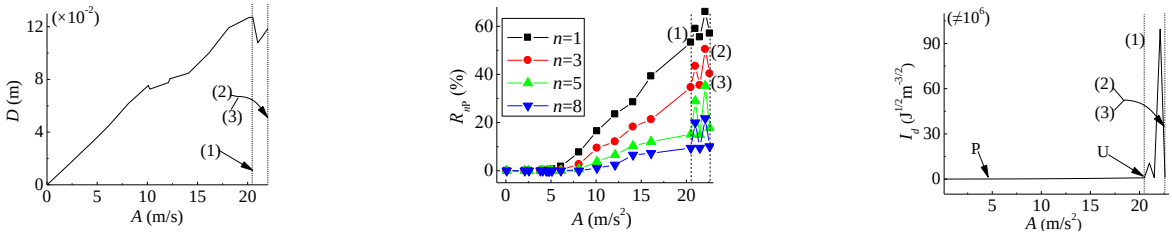

(a) The D-A curve (b) The R_{np}–A curve (c) The I_d-A curve

Fig. 10 The D-A, R_{np}–A and I_d-A curves

Note: The dotted lines (1), (2) and (3) correspond to the failure loads determined using the ESED-based, empirical and convergent criteria, respectively.

definiteness raises the question whether or not the failure of a few elements in the structure (a local failure of the structure) might result in the appearance of Point *U*; in other words, Point *U* might correspond to the local failure rather than the global failure of the structure. To address this question, the SED values of all the elements in Shell D40207 near to the failure load are plotted in Fig. 9(d). From Fig. 9(d), the SED values increase with *A*, but the SED values of a few elements increase much more obviously than do the other elements when *A* reaches a certain value. For instance, the SED value of the element 449 rockets at A=20.1 m/s^2. However, Fig. 9(b) shows that before A=21.0 m/s^2, I_d continuously and steadily increase until Point *U* appears, without an evident effect from the great SED value of the element 449 at A=20.1 m/s^2. Once more, it is verified that I_d is a structural parameter and can definitely demonstrate structural working characteristic, as well as the characteristic point *U* based on I_d presents the structural failure load, not the local failure load of the structure.

5.2 Rationality of the ESED-based criterion

In this section, the rationality of the ESED-based criterion is demonstrated in the comparison with two existing representative criteria. The first one is Zhi's criterion (Zhi *et al*. 2007) for the single layer spherical lattice shell which can be expressed as

$$C_s = 3.2\sqrt{(H/L)\left(100\left((\frac{D-D_e}{L})^2+(\frac{\varepsilon_a}{\varepsilon_u})^2\right)+R_{1p}^2+R_{8p}^2\right)} \quad (17)$$

where C_s is the structural damage index; H and L are the height and span of the shell, respectively; D is the maximum nodal displacement; D_e is the ultimate elastic displacement; ε_a is the structural average strain; ε_u is the ultimate strain of steel; R_{1p} and R_{8p} are the plastic ratios of the members.

The other one is the convergence criterion (Chong, 1993) in the FEA simulation, as expressed by Eq. (18)

$$TOF > \sqrt{\sum(Force\ Imbalances)^2},\quad TOD > \sqrt{\sum(u_i - u_{i-1})^2} \quad (18)$$

where *TOF* and *TOD* are the tolerance of force and the tolerance of displacement, respectively; u_i and u_{i-1} are the displacement values from two adjacent numerical iterations. It should be noted that the convergence criterion can calculate the dynamic collapse load only, but it could not determine the dynamic strength failure load.

Here, Shell D40207 under the harmonic excitation with 5 Hz frequency is once again taken as an example to examine the rationality of the ESED-based criterion expressed by Eq. (16), in comparison of the Zhi's criterion and convergence criteria of the FEA simulation. Corresponding, the key parameters in the criterion are the ESED parameter I_d, the maximum nodal displacement D and the structural yield level R_{np}. R_{np} is also called as the yield element ratio corresponding to the percentage of the members with n yield points among all the members consisting of the structure. Fig. 10 presents the relationships of D, R_{np} and I_d with the harmonic seismic amplitude A. The dotted lines (1), (2) and (3) indicate the failure loads

Table 3 The yield element ratios and the maximum displacements of the shells

Shell label	D (m)		R_{1P}		R_{3P}		R_{5P}		R_{8P}		Failure load (m/s^2)	
	ESED	**Zhi**	ESED	**Zhi**	ESED	**Zhi**	ESED	**Zhi**	ESED	**Zhi**	ESED	**Zhi**
D40203	1.15	**0.08**	0.97	**0.59**	0.85	**0.49**	0.65	**0.17**	0.54	**0.02**	31.50	**8.10**
D40205	0.11	**0.11**	0.71	**0.71**	0.62	**0.62**	0.32	**0.32**	0.20	**0.20**	18.50	**18.50**
D40207	0.14	**0.16**	0.59	**0.85**	0.38	**0.71**	0.18	**0.46**	0.11	**0.25**	12.50	**20.10**
D50063	1.71	**0.12**	0.83	**0.56**	0.77	**0.45**	0.59	**0.23**	0.47	**0.03**	64.20	**28.10**
D50065	1.07	**0.14**	0.93	**0.72**	0.87	**0.63**	0.78	**0.32**	0.63	**0.08**	76.50	**33.60**
D50067	0.57	**0.35**	0.90	**0.86**	0.89	**0.79**	0.81	**0.57**	0.61	**0.26**	69.00	**48.10**
D60063	2.46	**0.21**	0.84	**0.59**	0.78	**0.49**	0.63	**0.33**	0.49	**0.07**	68.90	**30.10**
D60065	0.28	**0.28**	0.85	**0.85**	0.81	**0.81**	0.67	**0.67**	0.44	**0.44**	53.00	**53.00**
D60067	0.50	**0.50**	0.83	**0.83**	0.66	**0.66**	0.33	**0.33**	0.10	**0.10**	34.80	**34.80**

Note: ESED denotes that the values calculated using the ESED criterion; Zhi (Zhi 2006) denotes that the values calculated using Zhi's criterion; R_{1p} denotes the yield element ratio for 1P; similarly, R_{3p}, R_{5p} and R_{8p} denote the yield element ratio for 3P, 5P and 8P, respectively; D is the maximum displacement.

predicted by the ESED-based criterion, Zhi's criterion and the convergence criterion, respectively. Fig. 10 verifies the rationality of the ESED-based criterion below.

Firstly, the ESED-based criterion exhibits the better robusticity than the convergence criterion and Zhi's criterion. In Fig. 10(a) and (b), the segments from Line (1) to Line (2) or (3) in the D-A and R_{np}-A curves are unstable and variable and even difficult to identify the tendency of the curves. Actually, the parameters D and R_{np} predicted by the convergence criterion and Zhi's criterion lie in the unstable and variable ranges of the respective curves. However, there is an evident characteristic point U in the I_d–A curve, as shown in Fig. 10(c), which has been captured by the ESED-based criterion. Specifically, before the characteristic point U, the I_d value keeps a stably increasing tendency with A. Therefore, the ESED-based criterion is able to predict a critical working state of the structure; in other words, the ESED-based criterion determines a boundary from a normal/stable working state to an unstable working state of the structure.

Secondly, the ESED-based criterion embodies reasonable conservation when compared with the convergence criterion and Zhi's criterion. It can be seen from Fig. 10 that the failure load predicted by the ESED-based criterion corresponds to the end of structural normal/stable working state, but the failure loads predicted by Zhi's criterion and the convergent criterion correspond to structural failure/unstable working state. Hence, the ESED-based criterion is reasonably conservative because the safe working state of a structure should be its normal/stable working state.

Lastly, the ESED-based criterion embodies more unified than the convergence criterion and Zhi's criterion, as implied in Fig. 10. For the convergence criterion, the maximum displacement D may not correspond to the same node and is a local parameter to a great extent. For Zhi's criterion, the structural yield level R_{np} may be not the same percentage of the members with n yield points among all the members consisting of the structure, besides the maximum nodal displacement D. Therefore, the ESED-based criterion might be a unified criterion for predicting structural failure load.

To further verify the rationality of the ESED-based criterion, Table 3 lists the failure loads of the shells predicted by the ESED-based criterion and Zhi's criterion. In addition, Table 3 also lists the maximum nodal displacements and the yield element ratios R_{np}.

Table 3 indicates that two criteria can give the same failure loads for some shells (i.e., D40205, D60065, D60067), implying that the ESED-based criterion is appropriate to predict the failure loads of shells subjected to seismic action. However, for the 1/3 rise-span shells, the ESED-based criterion and Zhi's criterion give out significantly different failure loads, maximum displacements and yield element ratios. From Table 3, it is also seen that, in terms of structural span, the maximum nodal displacement from Zhi's criterion are relatively small, less than 1/125 of the shell span. Besides, the mean value of the maximum nodal displacements is smaller than 1/250 of the shell span, when compared with a corresponding value of 1/59 from the ESED-based criterion. But, it seems difficult to judge which criterion is more rational from the difference between two criteria mentioned above. For this question, the following reasons are given to the judgment that the ESED-based criterion might be more rational than Zhi's criterion: (1) Zhi's criterion is mainly based on empirical and statistical judgment, while the ESED-based criterion is based on the characteristic point U of structural working state; (2) the maximum nodal displacement might be local in Zhi's criterion, while structural working state is global in the ESED-based criterion; (3) the ESED-based criterion considers both material and geometrical nonlinearities, whereas Zhi's criterion mainly deals with geometrical nonlinearity.

Overall, the ESED-based criterion could reflect more physical mechanisms than Zhi's criterion and the convergence criterion; besides, it can comprise both material and geometric nonlinearity. More importantly, the ESED-based criterion embodies more unified working characteristic of the whole structure than the other two criteria. Hence, the ESED-based criterion could bring more economic and rational prediction of the failure load for a shell, particularly for the shell with a higher rise-span ratio.

5.3 Application of the ESED-based criterion

The existing code for large-span spatial structures subjected to severe seismic action is greatly based on an empirical judgment on structural failure. In other words, structural failure as the reference to the design code is not mainly from mechanical judgment. Thus, the empirical-based design code has to pay a high economic price to obtain a safe design for large-span spatial structures. Therefore, there have been extensive research efforts in the field of structural engineering to pursue a mechanical-based criterion for structural anti-seismic design. The ESED-based criterion provides such a relatively mechanical basis for improving the existing design code of large-span spatial

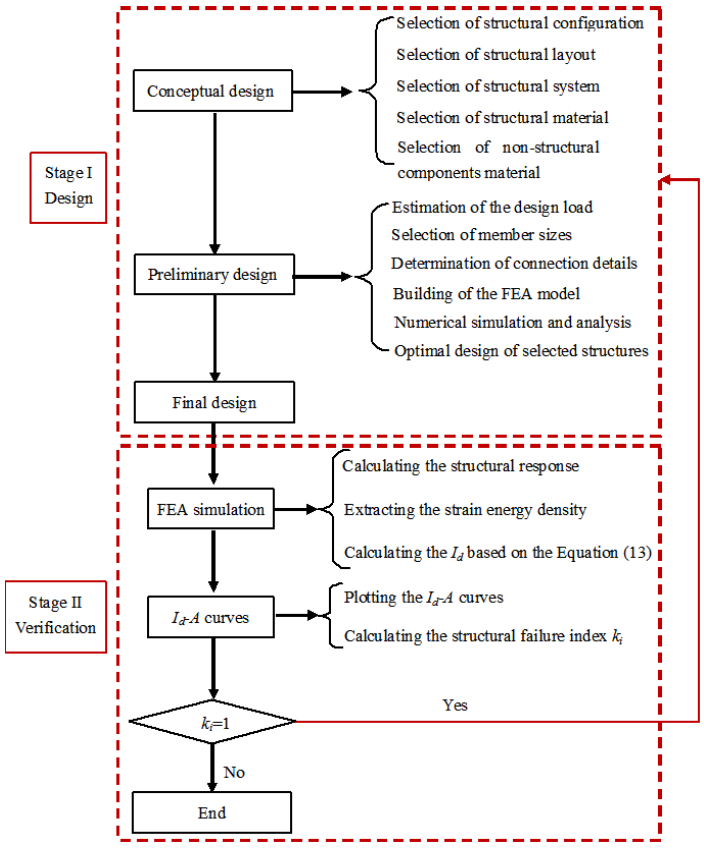

Fig. 11 The design process of shell structures based on the ESED criterion

structures subjected to severe seismic action. According to the Chinese design code (JGJ7-2010 2010), the design flowchart of shell structures using the ESED-based criterion is given in Fig. 11. It mainly includes two stages.

Stage I consists of conceptual design and preliminary design. The conceptual design is to select structural type and configuration, material, non-structural components, constraints, aesthetic expression, etc. The preliminary design is mainly to build structural model and to set both loading case and design load value.

Stage Ⅱ consists of the FEA simulation of the structural model built in Stage I, I_d-A curves and the determination of the failure load. The general FEA program is used to calculate the response of the structure under applied load; simultaneously, the SED values of all the elements are extracted as the database for the ESED-based criterion. Then, the relationship between I_d and the applied load is investigated and the structural failure index k_i is calculated using Eq. (16). Finally, if the load value corresponding to k_i and the design load value from the design code are within the allowable difference, the design process is finished, that is, the design scheme can satisfy the requirements of the design code; otherwise, the structural configuration needs to be modified until the load value corresponding to k_i meets the design load value.

6. Conclusions

The ESED method explores a novel way to analyze structural working behavior. An innovative parameter I_d derived in the ESED method conducts an investigation into the relationship between I_d and the peak acceleration A, which reveals a characteristic point of structural working state.

Then, a parameter k_i, defined as structural failure index, is proposed to determine the characteristic point. Thus, an ESED-based criterion is put forward to predict the seismic failure loads of shells. Numerical and experimental studies validate the ESED-based criterion.

Finally, the rationality, unity and applicability of the ESED-based criterion are assessed in comparison of the existing criteria for predicting the failure loads of single-layer spherical reticulated shells. The assessment indicates that the ESED-based criterion not only embodies more rational than the existing criteria, but also presents a possibility to establish a unified criterion for predicting the failure loads of various structures under a dynamic or static load.

Acknowledgments

The research for this paper was supported by Chinese National Natural Science Foundation (Grant No. 51608452 and Grant No. 51308465). The authors would like to thank all the staffs in Space Structure Research Center of Harbin Institute of Technology for their valuable suggestions and help.

References

Ba, P.F., Zhang, Y.G., Wu, J.Z. and Zhang, Z.H. (2015), "The failure criterion of single-layer spherical lattice shell based on kinetic energy", *Math. Probl. Eng*., **2015**, Article ID 485710.

Bai, Y., Yang, L. and Gong, L.F. (2015), "Elasto-plastic bearing capacity of four types of single-layer reticulated shell structures under fire hazards", *Int. J. Struct. Stab. Dyn.*, **15**(3), 1450051.

Bruno, L., Sassone, M. and Fiammetta, V. (2016), "Effects of the equivalent geometric nodal imperfections on the stability of single layer grid shells", *Eng. Struct*., **112**, 184-199.

Chong, V.L. (1993), "The behavior of laterally loaded masonry panels with openings", PhD Dissertation, University of Plymouth, Plymouth.

Chopra, A.K. (1995), *Dynamics of Structures*, Prentice Hall, New Jersey, California, USA.

Fan, F., Cao, Z.G. and Shen, S.Z. (2010), "Elasto-plastic stability of single-layer reticulated shells", *Thin. Wall. Struct*., **48**(10-11), 827-836.

Fan, F., Li, Y.G., Zhi, X.D. and Li, L. (2014), "Comparison of seismic response of single-layer reticulated dome under uniform and incoherence three-directional excitations", *Int. J. Steel Struct.*, **14**(4), 855-863.

Fan, F., Wang, D.Z., Zhi, X.D. and Shen, S.Z. (2010), "Failure modes of reticulated domes subjected to impact and the judgment", *Thin Wall. Struct.*, **48**(2), 143-149.

JGJ7-2010 (2010), Technical Specification for Space Frame Structures, Ministry of Housing and Urban-Rural of Development of the People's Republic of China, Bei Jing, China.

Kong, D.W., Fan, F. and Zhi, X.D. (2014), "Seismic performance of single-layer lattice shells with VF-FPB", *Int. J. Steel Struct.*, **14**(4), 901-911.

Li, Y.G., Fan, F. and Hong, H.P. (2014), "Effect of support flexibility on seismic responses of a reticulated dome under spatially correlated and coherent excitations", *Thin Wall. Struct*., **82**, 343-351.

Liu, C.G. and Li, H.J. (2010), "A novel method to calculate the dynamic reliability of space structures subjected to multi-dimensional multi-support excitations", *Int. J. Space Struct.*, **25**(1), 25-34.

Liu, W.Z. and Ye, J.H. (2014), "Collapse optimization for domes under earthquake using a genetic simulated annealing algorithm", *J. Constr. Steel. Res.*, **97**, 59-68.

Ma, H.H., Fan, F., Wen, P., Zhang, H. and Shen, S.Z. (2015), "Experimental and numerical studies on a single-layer cylindrical reticulated shell with semi-rigid joints", *Thin Wall. Struct*., **86**, 1-9.

Ma, J.L., Wu, C.Q., Zhi, X.D. and Fan, F. (2014), "Prediction of confined blast loading in single-layer lattice shells", *Adv. Struct. Eng*., **17**(7), 1029-1043.

Maria, J.F. and Chris, G.K. (2014), "Influence of pinching effect of exterior joints on the seismic behavior of RC frames", *Earthq. Struct.*, **6**(1), 89-110.

Nie, G.B., Zhi, X.D., Fan, F. and Dai, J.W. (2014), "Seismic performance evaluation of single-layer reticulated dome and its fragility analysis", *J. Constr. Steel. Res.*, **100**, 176-182.

Owen, D.R. and Hinto, E. (1980), *Finite Elements in Plasticity: Theory and Practice*. Pineridge Press Limited, Swansea, UK.

Paolacci, F. (2013), "An energy-based design for seismic resistant structures with viscoelastic dampers", *Earthq. Struct.*, **4**(2), 219-239.

Ramalingam, R. and Jayachandran, S.A. (2015), "Postbuckling behavior of flexibly connected single layer steel domes", *J. Constr. Steel Res.*, **114**, 136-145.

Shehata, E.A.R. and Toshiro, H. (2013), "Energy dissipation system for earthquake protection of cable-stayed bridge towers", *Earthq. Struct.*, **5**(6), 657-678.

Yan, J.C., Qin, F., Cao, Z.G., Fan, F. and Mo, Y.L. (2016), "Mechanism of coupled instability of single-layer reticulated domes", *Eng. Struct*., **114**, 158-170.

Yan, R.Z., Chen, Z.H., Wang, X.D., Xiao, X. and Yang, Y. (2014), "Calculation theory and experimental study of the K6 single-layer reticulated shell", *Int. J. Steel Struct.*, **14**(2), 195-212.

Ye, J.H., Zhang, Z.Q. and Chu, Y. (2011), "Strength behavior and collapse of spatial-reticulated structures under multi-support excitation", *Sci. Chin. Technol. Sci*., **54**, 1624-1638.

Ye, J.H., Zhang, Z.Q. and Chu, Y. (2011), "Strength failure of spatial reticulated structures under multi-support excitation", *Earthq. Eng. Vib.*, **10**(1), 21-36.

Yu, Z.W., Zhi, X.D., Fan, F. and Chen, L. (2011), "Effect of substructures upon failure behavior of steel reticulated domes subjected to the severe earthquake", *Thin Wall. Struct*., **49**, 1160-1170.

Zhai, X.M. and Wang, Y.H. (2013), "Modeling and dynamic response of steel reticulated shell under blast loading", *Shock Vib*., **20**(1), 19-28.

Zhi, X.D., Fan, F. and Shen, S.Z. (2007), "Failure mechanisms of single-layer reticulated domes subjected to earthquakes", *J. Int. Assoc. Shell Spatial Struct*., **48**(1), 29-44.

Zhi, X.D., Fan, F. and Shen, S.Z. (2010), "Elasto-plastic instability of single-layer reticulated shells under dynamic actions", *Thin Wall. Struct*., **48**, 837-845.

Zhong, J., Zhi, X.D. and Fan, F. (2016), "A dominant vibration mode-based scalar ground motion intensity measure for single-layer reticulated domes", *Earthq. Struct.*, **11**(2), 245-264.

Zhu, N.H. and Ye, J.H. (2014), "Structural vulnerability of a single-layer dome based on its form", *J. Eng. Mech.*, **140**(1), 112-127.

CC